# Consistent and accurate state evaluations in variable-density flow simulations

**By L. Shunn AND F. Ham**

## 1. Motivation and objectives

For the case of low-Mach number combustion where acoustic effects are considered unimportant, the variable-density equations for reacting flows can realize substantial efficiency gains relative to fully compressible formulations. In variable-density formulations, pressure and density are formally decoupled by defining the density through an equation-of-state (EOS) in terms of one or more transported scalars: $\rho = \rho(\phi_1, \phi_2, ...)$. The EOS may be given by an analytic expression, or as is common for complex reactive systems, it may be precomputed and tabulated as a function of the scalars.

When the variable-density equations are discretized and solved numerically, it is common to use a fractional-step formulation where a constant-coefficient Poisson equation for pressure is derived through a constraint on the divergence of $\rho u_i$ coming from the continuity equation. The resulting equation for pressure has the time derivative of the density as a source term, and is solved and used to correct the velocity field and enforce mass conservation discretely. For density ratios of approximately three or greater, instabilities are commonly encountered and resolved by largely ad hoc techniques whose effect on the solution cannot easily be quantified. For example, Pierce & Moin (2001, 2004) characterized the problem as "spurious heat release" related to inconsistencies between the mass and scalar transport, and resolved the instabilities by spatially filtering the computed $\partial\rho/\partial t$ source term several times. While this will not alter the mass in the simulation (assuming a conservative filter), it does have the effect of moving mass around in a way not called for by the governing equations. Forkel & Janicka (2000) performed temporal filtering of the density to stabilize their calculations. This introduces an additional complexity and hysteresis to the state equation whose effect is also difficult to quantify.

Other authors have reformulated the numerical method to solve a variable-coefficient Poisson system derived through a constraint on the velocity divergence coming from the energy equation. While these approaches stably support much higher density ratios, it appears necessary to relax the conservation properties of the scheme (Nicoud 2000), or allow the state to wander somewhat from the state equation (Pember *et al.* 1998).

In the present study the instability problem is resolved by recognizing that nonlinearities in the state equation can introduce a multi-scale resolution problem not supported by the grid. This problem can be largely resolved by simply evaluating the density (and other tabulated source terms) using an accurate subgrid representation.

## 2. Consistent state evaluations

### 2.1. *Numerical method*

The simulations presented in this brief are performed using a collocated, unstructured version of the algorithm of Pierce & Moin (2001). The algorithm employs a temporally-

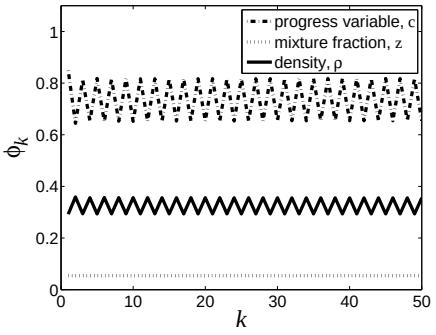


FIGURE 1. Scalars versus inner-iterations at a single spatial location in a non-convergent combustion simulation.

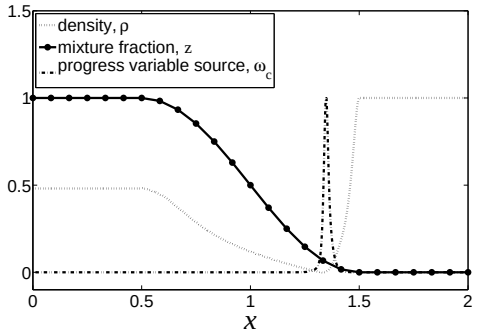


FIGURE 2. Mixture fraction, density, and product source term.

staggered variable arrangement in which velocity components are staggered in time with respect to density and other scalar variables. The velocity and scalars are implicitly advanced in time, and an iterative approach is used at each time level to repair linearization errors and enhance stability. The overall algorithm was implemented in the computer code CDP using unstructured node-based finite volume operators. Details of CDP's node-base operators are described elsewhere in this volume (Ham *et al.* 2006).

The salient features of the iteration process at each time step are as follows:

1. The scalar equation(s) are advanced in time. This yields $(\rho\phi)^{k+1}$, from which a provisional estimate for $\phi^{k+1}$ is obtained by $\widehat{\phi} = (\rho\phi)^{k+1}/\rho^k$.
2. The momentum equation is advanced to obtain provisional velocities: $\widehat{u_i}$.
3. The provisional scalar values are used to evaluate the density from the EOS: $\rho^{k+1} = f(\widehat{\phi})$.
4. The updated density is used to correct the scalar(s) to ensure primary conservation: $\phi^{k+1} = (\rho\phi)^{k+1}/\rho^{k+1}$.
5. A Poisson equation is solved for pressure corrections that satisfy the continuity equation, and the pressure and velocity fields are adjusted accordingly.
6. The process is repeated from step 1 and continued until convergence.

Linear stability analysis indicates that the above iterative approach is second-order accurate when at least two inner-iterations are employed (Pierce & Moin 2001). Additional iterations may improve the stability of the scheme, but do not increase the order of accuracy. When the scheme is applied to real combustion problems, however, it is generally not iterated to convergence. Normally, a fixed number of inner-iterations are performed (typically 3–5) and then the time step is considered to be "converged." Formal verification of the second-order behavior of the algorithm requires convergence of the system at each time step. For many of the combustion problems investigated, however, rigorous convergence of the scheme was not possible. For example, Fig. 1 shows the values of three scalar quantities sampled from one spatial location in a combustion simulation at successive inner-iterations of a single time step. In this example the density is obtained as a function of two transported scalars: the mixture fraction, $z$, and a reaction progress-variable, $c$. Clearly, the system is non-convergent irrespective of the number of inner-iterations used, presenting a serious impediment to verification.

### 2.2. *Source of instabilities*

These instabilities can be reproduced and their sources understood by studying much simpler problems. Consider, for example, the 1-D problem depicted in Fig. 2, which shows the mixture fraction, $z$, as a function of the spatial coordinate, $x$. Also shown are the density and product source term, $\omega_c$, which are consistent with non-premixed methane chemistry at slightly elevated pressures. An example computational grid is denoted by the solid symbols along the mixture fraction curve. Note that although the mixture fraction transition in the figure is reasonably resolved, the highly non-linear behavior of the density and source term would be grossly under-represented on this grid. Instabilities can develop as the under-resolved, non-linear features of the EOS are transported through the grid.

Consider the case of convective scalar transport (no diffusion) with the density given as a continuous function of one scalar, i.e.,

$$\frac{\partial \rho\phi}{\partial t} + \frac{\partial \rho u_i \phi}{\partial x_i} = 0, \qquad \rho = \rho(\phi). \tag{2.1}$$

Together with continuity,

$$\frac{\partial \rho}{\partial t} + \frac{\partial \rho u_i}{\partial x_i} = 0, \tag{2.2}$$

these equations are equivalent to passive scalar advection and a divergence-free velocity field, i.e.,

$$\frac{\partial \phi}{\partial t} + u_i \frac{\partial \phi}{\partial x_i} = 0, \qquad \frac{\partial u_i}{\partial x_i} = 0. \tag{2.3}$$

This continuous equivalence is exploited in some numerical approaches for multi-phase flow, such as the level set method, where Eq. 2.3 is discretized and solved. For the case of turbulent combustion, however, discrete conservation is considered important, so it is preferable to discretize and solve the conservative form of both scalar transport and continuity. Due to discretization errors, this equivalence is not realized discretely and manifests itself in some non-physical divergence in the velocity field.

One way to reduce this non-physical divergence can be seen by considering the leading truncation error associated with the second-order approximations normally used in discretizing Eqs. 2.1 and 2.2. Consider the 1-D case inside a control volume of size $\Delta x$. The volume integration of density associated with the time derivative in the continuity equation is

$$\frac{1}{\Delta x} \int_{-\Delta x/2}^{\Delta x/2} \rho(\phi) dx = \rho(\phi_0) + \frac{\Delta x^2}{24} \left[ \left.\frac{\partial \rho}{\partial \phi}\right|_{\phi_0} \left.\frac{\partial^2 \phi}{\partial x^2}\right|_0 + \left.\frac{\partial^2 \rho}{\partial \phi^2}\right|_{\phi_0} \left( \left.\frac{\partial \phi}{\partial x}\right|_0 \right)^2 \right] + O(\Delta x^4) \tag{2.4}$$

and the volume integration of density times the scalar associated with the time derivative in the scalar transport equation is

$$\begin{aligned} \frac{1}{\Delta x} \int_{-\Delta x/2}^{\Delta x/2} \rho(\phi)\phi dx = \rho(\phi_0)\phi_0 + \\ \frac{\Delta x^2}{24} \left[ \rho(\phi_0) \left.\frac{\partial^2 \phi}{\partial x^2}\right|_0 + 2 \left.\frac{\partial \rho}{\partial \phi}\right|_{\phi_0} \left( \left.\frac{\partial \phi}{\partial x}\right|_0 \right)^2 + \right. \end{aligned} \tag{2.5}$$

$$\left. \phi_0 \frac{\partial \rho}{\partial \phi} \right|_{\phi_0} \left. \frac{\partial^2 \phi}{\partial x^2} \right|_0 + \left. \phi_0 \frac{\partial^2 \rho}{\partial \phi^2} \right|_{\phi_0} \left( \left. \frac{\partial \phi}{\partial x} \right|_0 \right)^2 \Bigg] + O(\Delta x^4).$$

By introducing a higher-order reconstruction of density in the control volume, it is clear that the truncation errors associated with both of these approximations can be reduced. For example, introducing a more accurate approximation for the density in the control volume, $\widehat{\rho}$:

$$\widehat{\rho} = \rho(\phi_0) + \frac{\Delta x^2}{24} \left[ \left. \frac{\partial \rho}{\partial \phi} \right|_{\phi_0} \left. \frac{\partial^2 \phi}{\partial x^2} \right|_0 + \left. \frac{\partial^2 \rho}{\partial \phi^2} \right|_{\phi_0} \left( \left. \frac{\partial \phi}{\partial x} \right|_0 \right)^2 \right] \tag{2.6}$$

removes all of the second-order error in Eq. 2.4 and two of the four second-order terms in Eq. 2.5. Numerical experiments indicate that the removal of the curvature term involving $\partial^2 \rho / \partial \phi^2$ is particularly important, as this term is normally dominant.

The extension of this more accurate approximation of the density to multiple dimensions and unstructured grids is presented in the next section.

### 2.3. *Tetrahedral quadrature*

The purpose of this section is to develop a family of optimized quadrature rules that can be used to efficiently evaluate volume-averaged state quantities in reactive simulations. Determining quadrature points for volume integration has been the subject of many studies; see the reviews of Cools & Rabinowitz (1993) and Cools (1999) for details. Accurate and efficient quadrature points can be generated by the recursive application of 1-D Gaussian quadrature, referred to as the product Gaussian rule (see Stroud 1971). When the product Gaussian rule is applied to tetrahedra, however, it results in an unpleasant asymmetry (and presumable inefficiency), clustering the points near one of the vertices.

The product Gaussian rule implicitly assumes an underlying structured hexagonal grid for the point locations. This grid samples a hexagonal space more or less uniformly. For tetrahedra, however, the structured hexagonal grid is inappropriate. A more natural grid for tetrahedra is that obtained by the hexagonal close-packed structure. Hexagonal close-packing is the arrangement obtained by packing spheres of equal size in the most efficient manner, such that each sphere (not on the boundary) touches its 12 nearest neighbors. In the present study we describe a method for developing quadrature points for tetrahedra based on parameterizing the point locations in terms of an underlying hexagonal close-packed grid, and then optimizing the precise point locations and weights to reduce the truncation error in the quadrature approximation. Such an approach results in a family of symmetric rules for tetrahedral integration where the number of integration points progresses as $n_p = 1$, 4, 10, 20, 35, 56, etc.

The integration of the function $f(x)$ over the tetrahedron $\Omega$ with volume $V_\Omega$ is defined

$$\int_\Omega f(x) dV = V_\Omega \left( \sum_{i=1}^{n_p} w_i f(x_i) + O(\delta^p) \right), \tag{2.7}$$

where $\delta$ is a length scale associated with the tetrahedron (e.g., the longest edge length), and $p$ is the order of the integration. The integration points (or quadrature points) $x_i$ are defined in terms of the four vertices of the tetrahedron $X_1, X_2, X_3, X_4$ as

$$x_i = \sum_{j=1}^{4} a_{i,j} X_j. \tag{2.8}$$

An integration scheme of this sort should have the following desirable properties (adapted from Vavasis 1998):

1. The scheme is optimal in some sense, e.g., minimizing truncation error.
2. It is symmetric, i.e., the scheme is independent of vertex ordering or the rule is invariant under affine maps of the tetrahedron to itself.
3. The weights are all positive: $w_i \geq 0$.
4. The quadrature points are all interior to the tetrahedron: $a_{i,j} \geq 0$.

The following integration schemes were developed by parametrizing the integration point locations in terms of the vectors of the unit equilateral tetrahedron scaled by $\delta$

$$X_1 = \delta\left(-\frac{1}{2}, -\frac{\sqrt{3}}{2}, -\frac{\sqrt{6}}{12}\right)$$
$$X_2 = \delta\left(\frac{1}{2}, -\frac{\sqrt{3}}{2}, -\frac{\sqrt{6}}{12}\right)$$
$$X_3 = \delta\left(0, \frac{\sqrt{3}}{3}, -\frac{\sqrt{6}}{12}\right)$$
$$X_4 = \delta\left(0, 0, \frac{\sqrt{6}}{4}\right)$$

and comparing the Taylor series expansion at the points to the exact integration of the Taylor series over the tetrahedron. The coefficients of successive powers of $\delta$ produce a series of non-linear equations that can be set equal to zero to solve for the positions and weights. When it was not possible to completely eliminate the truncation error at the highest level, then the error can be minimized in a least-squares sense, assuming the partial derivatives are all of equal magnitude. When more than one solution is found satisfying all four of the previously mentioned criteria, then the solution is considered to be the one with minimum least-squares truncation error.

The parameterization of the points exploits the tetrahedral symmetry by arranging the points as close-packed spheres and writing the sphere locations as linear combinations of the above vectors. Once the optimal solutions have been obtained, the point locations and weights are assembled and stored in a computer library for efficient implementation in numerical applications. The optimized rules are shown in Fig. 3, and their properties are summarized in Table 1.

## 3. Results

### 3.1. *1-D example problem*

The 1-D combustion problem shown schematically in Fig. 4 has been designed to demonstrate the impact of EOS evaluations on a flow simulation. Here an initial transition from fuel ($z = 1$) to oxidizer ($z = 0$) is imposed and allowed to evolve subject to diffusive mixing. A constant reference-frame velocity $u_{RF}$ can be supplied to translate the entire system through the computational grid.

For this problem, a polynomial state-relationship of the form

$$\rho = 2z + (1 - z)^{18} \tag{3.1}$$

is used to describe the density. This EOS exhibits strong non-linear behavior in the region

TABLE 1. Tetrahedral quadrature rules.

| Rule | Points | Order of Accuracy |
|---|---|---|
| 1 | 1 | $O(\delta^2)$ |
| 2 | 4 | $O(\delta^3)$ |
| 3 | 10 | $O(\delta^4)$ |
| 4 | 20 | $O(\delta^6)$ |
| 5 | 35 | $O(\delta^7)$ |
| 6 | 56 | $O(\delta^9)$ |

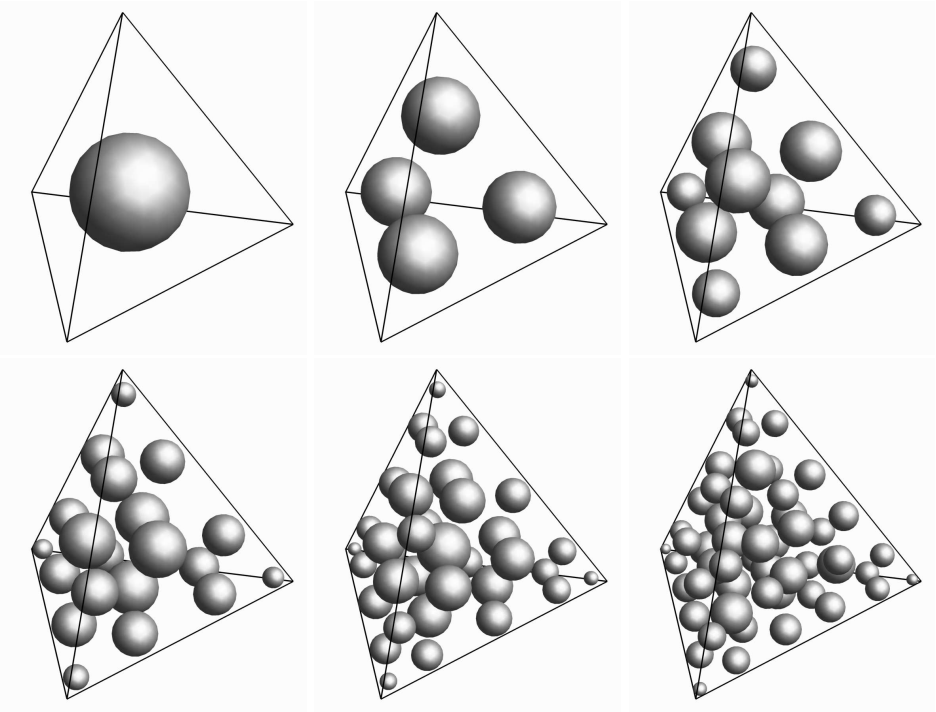

FIGURE 3. Tetrahedral integration quadrature point locations and weights. Top row (left to right): 1-, 4-, and 10-point rules. Bottom row (left to right): 20-, 35-, and 56-point rules.

$z \leq 0.2$ (see Fig. 5), and is indicative of the general behavior expected in non-premixed combustion systems. In particular, the density minimum around $z \approx 0.12$ suggests a region of reaction and heat release caused by the mixing of relatively dense fuel at $z = 1$ with moderately dense (preheated) air at $z = 0$.

As the fuel front in Fig. 4 diffuses, the low-density reactive region broadens and forces mass out of the right-hand side of the domain. The velocity at the exit, $u_{out}$, can be used

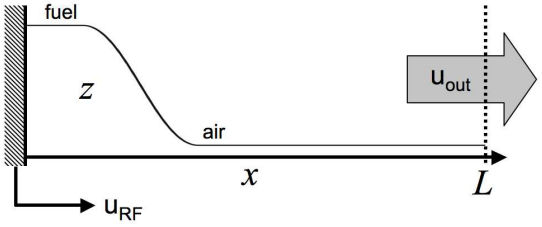


FIGURE 4. 1-D combustion problem.

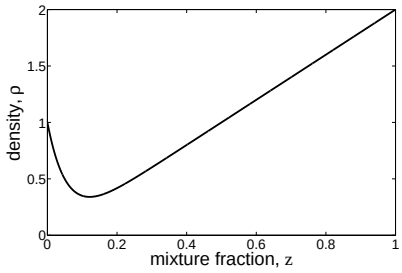


FIGURE 5. Model reactive EOS.

to monitor the global rate-of-change of mass in the system:

$$(u_{out} - u_{RF}) = \frac{-1}{\rho_{x=L}} \frac{d}{dt} \int_0^L \rho dx. \tag{3.2}$$

Here the outlet velocity is used to gauge the effectiveness of the density evaluations.

The 1-D diffusion problem was solved numerically using two different EOS-evaluation methods. In the first method, the mean density at a node is computed by simply evaluating the EOS using the mean mixture fraction value for that node. This method is referred to as "node evaluations." In the second approach, the independent function ($z$ in this case) is reconstructed linearly and continuously in the polyhedral region around each grid node. Each polyhedral control volume is then tessellated into tetrahedral subvolumes involving a combination of nodes, vertices, edges, and faces. A quadrature rule is applied within each subvolume to accurately integrate the state equation in space and construct an appropriate approximation to the density. This evaluation technique is referred to as "tetrahedral integration" (TI). 128 points in $x$ were used in all of the simulations, and the most accurate (56-point) quadrature rule was applied in the TI evaluations.

Figs. 6 and 7 show numerical solutions to the 1-D diffusion problem with reference-frame velocities of $u_{RF} = 0$ and $u_{RF} = 0.2$, respectively. Solutions using node evaluations and the TI method are compared in each figure. Three cases, denoted as (a), (b), and (c), were run for each EOS-evaluation technique. In case (a), the EOS (Eq. 3.1) was evaluated analytically to compute the density. In cases (b) and (c), the EOS was interpolated linearly from a grid of uniformly-spaced points in mixture-fraction space. Case (b) used 101 points in $z$ ($\Delta z = 0.01$), and case (c) used 51 points in $z$ ($\Delta z = 0.02$). Cases (b) and (c) are of practical interest due to the widespread use of tabulated state-relationships in industrial computations. Interpolation of the EOS at these $z$-resolutions is not unreasonable. The maximum and average errors in the density for case (b) are $\epsilon_{max} = 3.5 \times 10^{-3}$ and $\epsilon_{avg} = 1.5 \times 10^{-4}$. For case (c) the errors are approximately four times larger: $\epsilon_{max} = 1.3 \times 10^{-2}$ and $\epsilon_{avg} = 6.0 \times 10^{-4}$.

At the beginning of the simulation, the outlet velocity starts from some initial value dictated by the rate of diffusion and decays smoothly as the mixture fraction gradient decreases. This behavior is captured very well with both EOS-evaluation techniques when the analytic EOS is used to compute the density, as indicated in case (a) shown in Figs. 6 and 7. When linear interpolation is used to evaluate the EOS, however, interpolation errors cause unphysical oscillations in the velocity. These errors are clearly shown in cases (b) and (c) of Figs. 6 and 7. The node-based EOS evaluations are particularly susceptible to these errors.

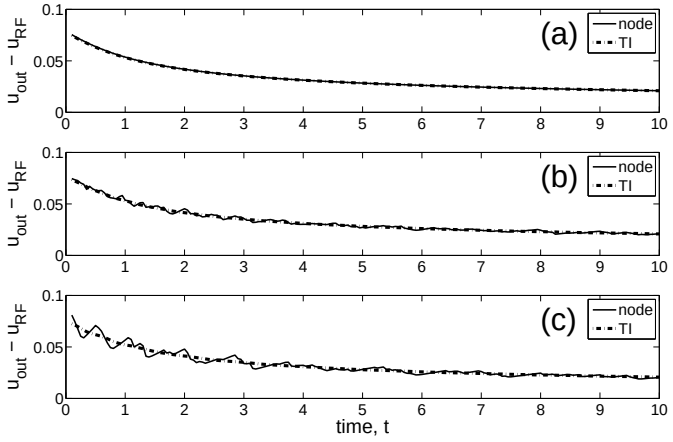


FIGURE 6. 1-D combustion problem with reference-frame velocity $u_{RF} = 0.0$. (a) analytic EOS evaluation, (b) linear interpolation $\Delta z = 0.01$, (c) linear interpolation $\Delta z = 0.02$.

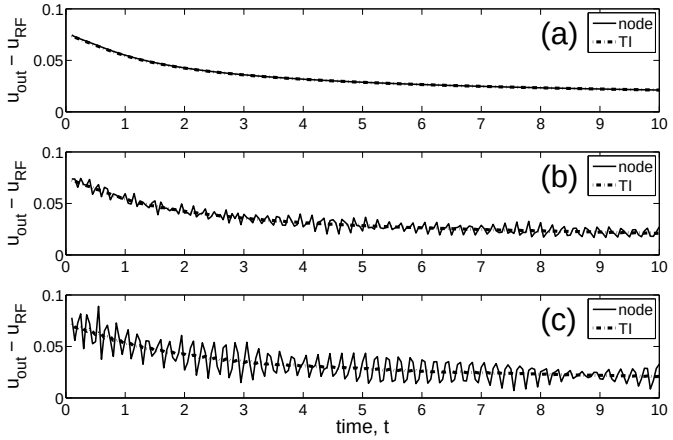


FIGURE 7. 1-D combustion problem with reference-frame velocity $u_{RF} = 0.2$. (a) analytic EOS evaluation, (b) linear interpolation $\Delta z = 0.01$, (c) linear interpolation $\Delta z = 0.02$.

To examine the cause of the unphysical oscillations, consider the evolution of the stoichiometric mixture fraction value, $z_{st}$. This value indicates the ratio of fuel to air that leads to chemical reactions, and can be loosely identified in this example as the density minimum in Fig. 5. As the flow evolves, the location of $z_{st}$ (and the corresponding nonlinear density region) moves through the computational grid under the effects of diffusion and reference-frame translation. When the EOS is under-resolved on the computational grid, this can lead to subtle errors in the instantaneous density field. These errors, when summed globally, lead to fluctuations with respect to time in the total amount of mass contained within the computational domain. In pressure projection methods, any erroneous mass is instantaneously removed from the system by adjusting the pressure and velocity to "correct" the global mass-balance of the system. As a consequence, spurious

density fluctuations give rise to spurious velocity and pressure fluctuations. The velocity and density in turn influence the evolution of the scalar field in a highly non-linear manner, further compounding the errors. The end result is that small errors in the EOS evaluation can amplify and lead to very large errors in the velocity and scalar fields.

Another way to explain these errors is to consider the implications of the piecewise-linear EOS used in cases (b) and (c). This representation is characterized by discontinuous first derivatives and undefined second derivatives of the density in mixture-fraction space. Examination of Eqs. 2.4 and 2.5 shows that these derivative terms are important for accurate approximation of the density. Neglecting these terms, as is done with node evaluations, can lead to large discrepancies in the numerical results.

The TI method is more resistant to this type of error because the TI-evaluated density reflects a subgrid average over the control volume, including features of the EOS that are not resolved on the computational grid. Small oscillations are still observed in the TI results, but the errors remain small and do not overwhelm the physics as in the case of the node evaluations.

### 3.2. *2-D example problem*

In more complex systems, EOS-evaluation errors can lead to significant errors in the time evolution of the flow, including the development of spurious flow structures and unphysical mixing. This is demonstrated through the 2-D problem shown in Fig. 8. The initial configuration is similar to the classical Rayleigh-Taylor mixing problem, however, the density is given by the "reactive" EOS used in the previous example (Eq. 3.1). As the initial disturbance evolves under the influence of gravity, the low-density region around $z_{st}$ is confined to a thin region around the fuel-oxidizer interface. Discretely representing these highly complex mixing patterns is a challenging computational problem.

Fig. 8 compares the time evolution of the 2-D mixing problem using node-based density evaluations and the TI method. Simulation results on four different grids are presented to show the effects of grid refinement on the solution and to give a point of comparison to judge the physicality of the coarse-grid solutions. For each EOS-evaluation method, the coarsest solution is shown in the left-most column of the figure matrix, and time increases from top to bottom. The most accurate (56-point) quadrature rule was applied for all evaluations in the TI computations. A non-dimensional viscosity of $\mu = 8.0 \times 10^{-4}$ was used in all cases, while the mixture fraction diffusivity was set to zero.

After only a short integration time, distinct differences emerge between the two EOS-evaluation methods. These differences are particularly pronounced on the coarser grids shown in Fig. 8. In the case of the node-based evaluations, the interface develops unphysical corrugations that numerically amplify as the solution progresses. After some time, the flowfield is contaminated with spurious flow structures evolving from an unphysical mixing-history. The coarse-grid results for the TI method, while still unresolved on the computational grid, tend to better preserve the characteristics and appearance of the resolved solutions. The difference between the two methods is clearly noticeable in Fig. 9, which shows the long-time evolution of the flowfield on a $50 \times 150$ grid. The different evaluation techniques are shown side-by-side with a more resolved solution for comparison purposes.

### 3.3. *Adaptive tetrahedral integration*

The hierarchical nature of the quadrature rules shown in Fig. 3 lends itself naturally to an adaptive EOS-evaluation procedure. Such an adaptive approach should efficiently focus additional quadrature work only where it is needed and apply lower-order methods

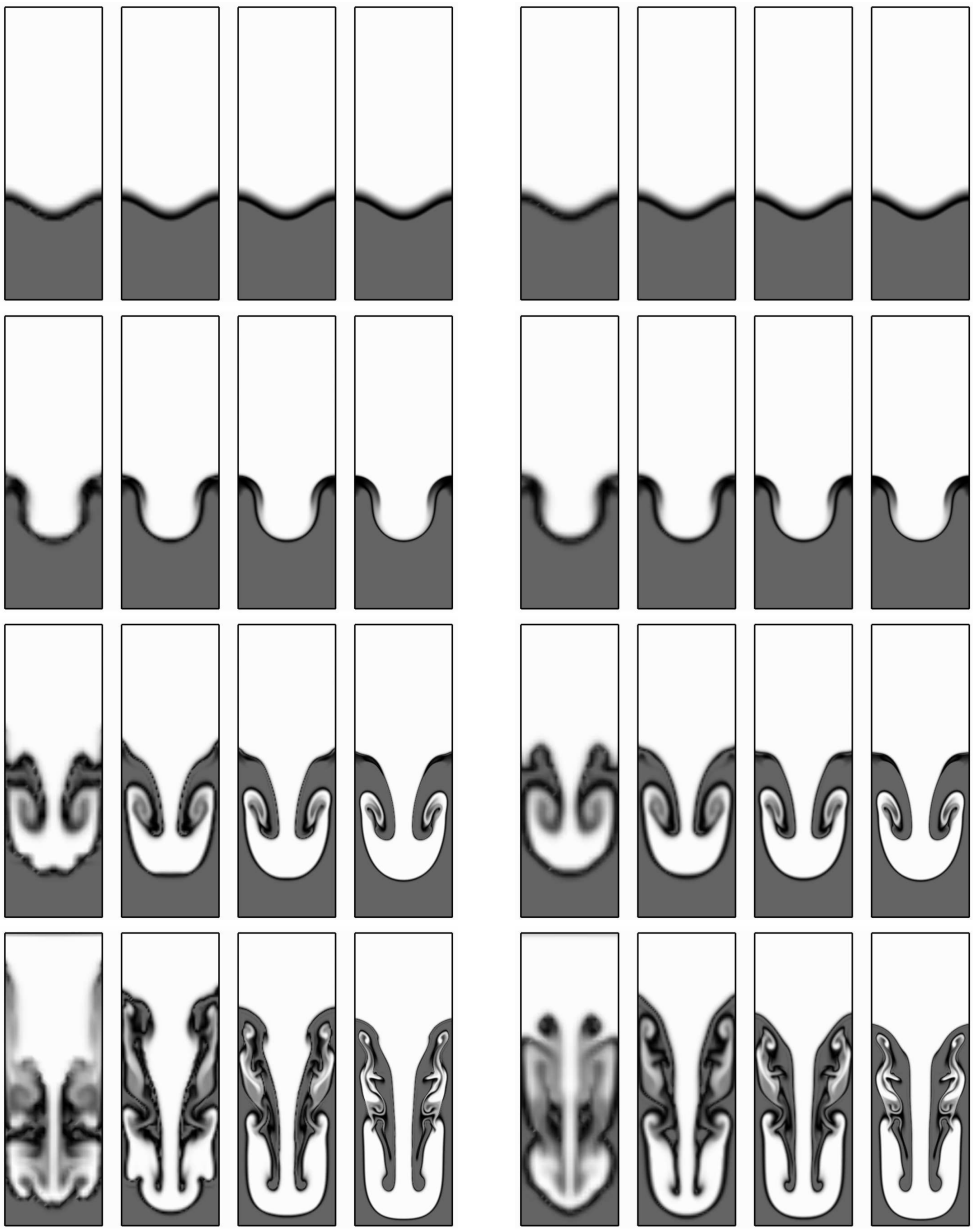

FIGURE 8. 2-D Rayleigh-Taylor instability. The left figures use node EOS-evaluations, and the right figures use TI 56-point EOS-evaluations. (top to bottom) $t = 0, t = 1.56, t = 3.08, t = 4.64$. (left to right) $25 \times 75$, $50 \times 150$, $100 \times 300$, $200 \times 600$ grids.

in regions that do not demand special treatment. One implementation strategy would be to adaptively select the quadrature rule based on the local spatial gradient of the scalar field. A computational cell that spans a large region of scalar-space would, for example, select a high-order, multi-point quadrature rule, whereas a cell with relatively homogeneous composition might only require a one-point evaluation. The minimum and

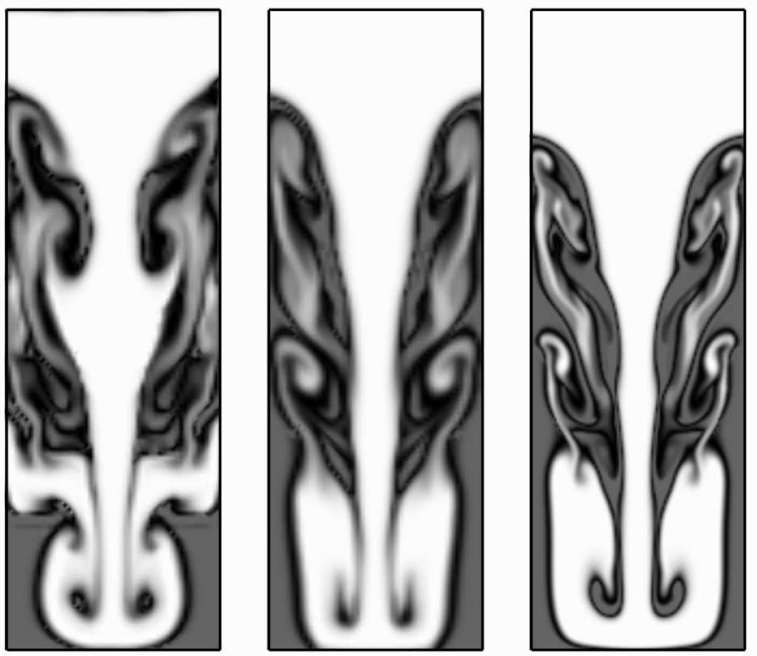

FIGURE 9. 2-D Rayleigh-Taylor instability at $t = 5.2$. (left to right) Node evaluations on $50 \times 150$ grid, TI 56-point evaluations on $50 \times 150$ grid, TI 56-point evaluations on $100 \times 300$ grid.

maximum values of the scalars at the vertices of tetrahedral subvolumes is a natural choice for gradient estimation in such a method.

The adaptive method described above has been applied to the 2-D Rayleigh-Taylor mixing problem (see Fig. 10). The criterion for rule selection in this example required at least one quadrature point per $\Delta z$ of 0.005. The time evolution of the solution is shown in Fig. 10. The upper figures show the evolution of the density, and the lower figures show the number of quadrature points used per subvolume. It is clearly seen that the bulk of the EOS-evaluation work is concentrated in the thin interface region of the solution. Fig. 11 compares the solution using the adaptive procedure with that obtained by universally applying the 56-point quadrature rule. The solutions are virtually indistinguishable.

The total execution time of the simulations was monitored for the $100 \times 300$ grid case, and the results are presented in Table 2. In all of the simulations, a sufficient number of inner-iterations was performed at each time level to converge the maximum density difference $|\rho^{k+1} - \rho^k|$ to less than $1.0 \times 10^{-6}$. Using TI with the 56-point quadrature rule incurred an increase of approximately 20% in the total execution time compared to node-based density evaluations. The adaptive TI method was the least computationally expensive approach. In this case, the extra EOS-evaluation work was offset by a decrease in the number of inner-iterations per time step and multi-grid cycles per Poisson-solve required to achieve the given levels of density and pressure convergence, respectively.

## 4. Summary

A method for consistent and accurate EOS evaluations in variable-density flow simulations has been developed and implemented. Various example problems were studied that

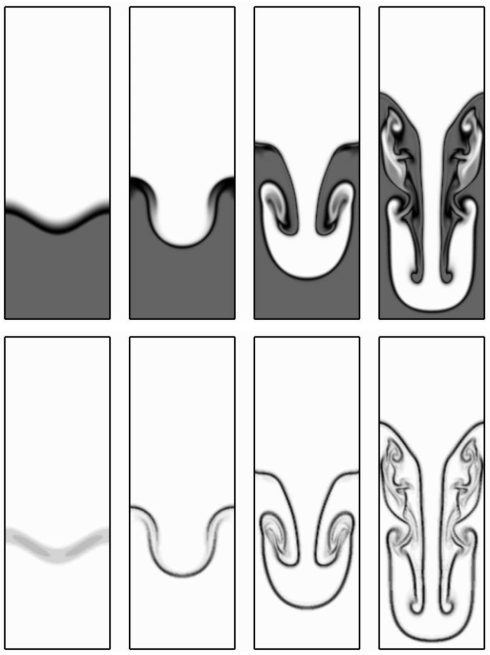

FIGURE 10. 2-D Rayleigh-Taylor instability on $100 \times 300$ grid using adaptive TI evaluations. Density on top, number of quadrature points per subvolume on bottom. (left to right) $t = 0$, $t = 1.56$, $t = 3.08$, $t = 4.64$.

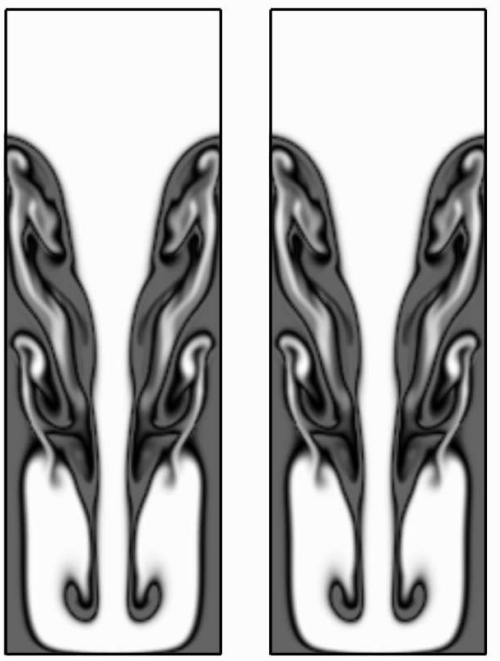

FIGURE 11. 2-D Rayleigh-Taylor instability on $100 \times 300$ grid at $t = 5.2$. (left to right) TI adaptive, TI 56-point.

TABLE 2. Execution time of simulations.

| Method | Time Steps | Total Time (min) | Average no. of Inner-Iterations | MG Cycles per Iteration |
|---|---|---|---|---|
| node | 1120 | 180 | 40.1 | 12.3 |
| TI 56-point | 1120 | 211 | 34.1 | 9.05 |
| TI adaptive | 1120 | 178 | 34.5 | 9.00 |

demonstrate that under-resolving the EOS can lead to numerical instabilities and unphysical flow features. A hierarchy of symmetric quadrature rules for tetrahedral volume integration was developed and used to efficiently integrate the EOS in fluid dynamics simulations. The new method, termed tetrahedral integration (TI), was shown to reduce EOS-evaluation errors, mitigate many of the undesirable numerical artifacts that result from other techniques, and produce a more physical evolution of the flowfield. The extra cost of the TI method is offset by better convergence and stability properties of the numerical solution.

**Acknowledgments**

This work was supported by the U.S. Department of Energy through the Advanced Simulation and Computing (ASC) program.

REFERENCES

Cools, R. 1999 Monomial cubature rules since "Stroud": a compilation — part 2. *J. Comput. Appl. Math.* **112**, 21–27.

Cools, R. & Rabinowitz, P. 1993 Monomial cubature rules since "Stroud": a compilation. *J. Comput. Appl. Math.* **48**, 309–326.

Forkel, H. & Janicka, J. 2000 Large-eddy simulation of a turbulent hydrogen diffusion flame. *Flow, Turb. Comb.* **65**, 163–175.

Ham, F., Mattsson, K. & Iaccarino, G. 2006 Accurate and stable finite volume operators for unstructured flow solvers. *Annual Research Briefs 2006* Center for Turbulence Research, Stanford University, NASA Ames.

Nicoud, F. 2000 Conservative high-order finite-difference schemes for low-Mach number flows. *J. Comput. Phys.* **158**, 71–97.

Pember, R. B., Howell, L. H., Bell, J. B., Colella, P., Crutchfield, C. Y., Fiveland, W. A. & Jessee, J. P. 1998 An adaptive projection method for unsteady, low-Mach number combustion. *Comb. Sci. Tech.* **140** (1-6), 123–168.

Pierce, C. D. & Moin, P. 2001 Progress-variable approach for large-eddy simulation of turbulent combustion. PhD thesis, Stanford University.

Pierce, C. D. & Moin, P. 2004 Progress-variable approach for large-eddy simulation of non-premixed turbulent combustion. *J. Fluid Mech.* **504**, 73–97.

Stroud, A. H. 1971 *Approximate calculation of multiple integrals*. Englewood Cliffs, NJ: Prentice-Hall.

Vavasis, S. A. 1998 Quadrature over tetrahedra. `http://www.cs.cornell.edu/home/vavasis/quad.html`. Accessed June 2006.